μSR and inelastic neutron scattering investigations of the noncentrosymmetric antiferromagnet $CeNiC_2$

A. Bhattacharyya,[1,2,*] D. T. Adroja,[1,2,†] A. M. Strydom,[2] A. D. Hillier,[1] J. W. Taylor,[1] A. Thamizhavel,[3] S. K. Dhar,[3] W. A. Kockelmann,[1] and B. D. Rainford[4]

[1]*ISIS Facility, Rutherford Appleton Laboratory, Chilton, Didcot Oxon OX11 0QX, United Kingdom*

[2]*Highly Correlated Matter Research Group, Physics Department, University of Johannesburg, P.O. Box 524, Auckland Park 2006, South Africa*

[3]*Tata Institute of Fundamental Research, Homi Bhabha Road, Colaba, Mumbai 400005, India*

[4]*Department of Physics, Southampton University, Southampton S09 5NH, United Kingdom*

(Received 6 March 2014; revised manuscript received 24 July 2014; published 8 August 2014)

The magnetic state of the noncentrosymmetric antiferromagnet $CeNiC_2$ has been studied by magnetic susceptibility, heat capacity, muon spin relaxation (μSR), and inelastic neutron scattering (INS) measurements. $CeNiC_2$ exhibits three magnetic phase transitions at $T_{N_1} = 19.5$ K, $T_{N_2} = 10$ K, and $T_{N_3} = 2.5$ K. The presence of long-range magnetic order below 20 K is confirmed by the observation of oscillations in the μSR spectra between 10 and 20 K and a sharp increase in the muon depolarization rate. INS studies reveal two well-defined crystal electric field (CEF) excitations around 8 and 30 meV. INS data have been analyzed using a CEF model and the wave functions were evaluated. We also calculated the direction and magnitude of the ground state moment using CEF wave functions and compare the results with that proposed from the neutron diffraction. Our CEF model correctly predicts that the moments order along the b axis (or y axis) and the estimated magnetic moment is $0.687(5)\mu_B$, which is higher than the moment observed from the neutron diffraction ($0.25\mu_B$/Ce). We attribute the observed reduced moment due to the Kondo screening effect.

DOI: 10.1103/PhysRevB.90.054405 PACS number(s): 75.10.Dg, 75.30.Gw, 75.30.Mb, 75.20.Hr

I. INTRODUCTION

A rich variety of novel phenomena is perceptible in Ce-based strongly correlated electron systems due to the duality between the localized and the itinerant nature of f electrons, for example, heavy electron and mixed valence behavior, Kondo insulator or semiconductors, unconventional superconductivity, spin- and charge-density waves, and spin and charge gap formations [1–6]. Recently metal-insulator transitions and an unexpectedly high temperature magnetic phase transition in an orthorhombic Ce materials class have attracted much interest [7,8].

$RNiC_2$ (R = rare earth) compounds crystallize in the noncentrosymmetric (NCS) orthorhombic $CeNiC_2$-type structure (space group $Amm2$) in which a mirror plane is missing along the c axis [9]. Diverse ground states such as the superconducting, antiferromagnetic (AFM)/ferromagnetic (FM), and the charge-density-wave (CDW) state have been reported so far in $RNiC_2$ (R = La, Ce, Pr, Sm, Gd, Tb, and Er), reflecting the competition among different electronic states [9–12]. Structural phase transitions have yet to be reported in these compounds, and hence the spin and charge ordering phenomena in $RNiC_2$ compounds are thus native to the NCS crystal structure. $LaNiC_2$ is a superconductor below about 2.7 K [13,14]. The absence of an inversion center is believed to give rise to mixed superconducting pairing state (combination of s-wave singlet and p-wave triplet) in NCS superconductors. It has been argued that heavy fermion effects are not significant except perhaps for R = Ce (on the other hand, mixed valence effects are significant for $SmNiC_2$ compound). Murase *et al.* [12] found that rare-earth intermetallic compounds $RNiC_2$ with R = Nd, Sm, Gd, and Tb show anomalous temperature dependences of electrical resistivity and lattice constants [12]. They proposed that these anomalies are attributed to CDW transitions. X-ray scattering studies of $SmNiC_2$ reveal satellite peaks corresponding to an incommensurate wave vector (0.5,0.52,0) below 148 K at which the resistivity shows an anomaly, signaling the development of a charge-density wave [15]. The rare-earth local moments order antiferromagnetically in most of the $RNiC_2$ compounds (apart from R = Pr), and $SmNiC_2$ undergoes a first-order ferromagnetic transition at $T_C = 17.5$ K [15,16]. Motoya *et al.* studied the neutron diffraction experiment on a $CeNiC_2$ compound and suggested a transition from an incommensurate to a commensurate antiferromagnetic order [10]. Those results indicate that $RNiC_2$ compounds having various magnetic orders are promising candidates for the systematic investigation of the interplay of CDW and magnetic order. In this system, nickel atoms are nonmagnetic and rare-earth elements mainly contribute to the magnetic properties, showing the character of local magnetic moments interacting through the Ruderman-Kittel-Kasuya-Yosida (RKKY) interaction. The magnetic properties of the $RNiC_2$ series are affected strongly by the orthorhombic crystalline electric field (CEF).

In this paper we report a detailed investigation on $CeNiC_2$ by dc magnetic susceptibility (χ), isothermal magnetization (M), heat capacity (C_P), neutron diffraction, muon spin relaxation (μSR), and inelastic neutron scattering (INS) measurements. Below 20 K a sharp anomaly is observed in our $\chi(T)$ and $C_P(T)$ data, which corresponds to a transition from the paramagnetic (PM) to AFM state. $C_P(T)$ data also show a second anomaly around 2.5 K and a further weak anomaly near 10 K. The presence of long-range magnetic order is also revealed by μSR measurements, where oscillations are

*amitava.bhattacharyya@stfc.ac.uk
†devashibhai.adroja@stfc.ac.uk

observed in the spectra below 20 K. A doublet ground state is inferred both from $C_P(T)$ and INS data. INS reveals two well-defined CEF excitations at 8 and 30 meV, indicating the localized nature of the $4f$ electrons in $CeNiC_2$.

II. EXPERIMENTAL DETAILS

Polycrystalline samples of $CeNiC_2$ and $LaNiC_2$ were prepared by arc melting of the constituent elements (Ce: 99.999 wt %; La: 99.999 wt %; Ni: 99.999 wt %; C: 99.999 wt %) in an argon atmosphere on a water cooled copper hearth. After being flipped and remelted several times, the buttons were wrapped in tantalum foil and annealed at 1000 °C for 168 h under a dynamic vacuum of nearly 10^{-6} Torr. Powder x-ray diffraction measurements were carried out using a Panalytical X-Pert Pro diffractometer. Magnetic susceptibility measurements were made using a magnetic property measurement system (MPMS) superconducting quantum interference device (SQUID) magnetometer (Quantum Design). Heat capacity measurements were performed by the relaxation method in a Quantum Design physical properties measurement system (PPMS).

The muon spin relaxation and inelastic neutron scattering experiments were carried out at the ISIS Pulsed Neutron and Muon Facility of the Rutherford Appleton Laboratory, United Kingdom. To check the phase purity of the samples, room-temperature neutron diffraction measurements were carried out using a General Materials (GEM) time-of-flight (TOF) diffractometer. The INS measurements were carried out on the time-of-flight MARI spectrometer between 4.5 and 100 K. The powder samples were wrapped in thin Al foil and mounted inside a thin-walled cylindrical Al can, which was cooled down to 4.5 K inside a top-loading closed cycle refrigerator with helium exchange gas around the sample. Incident neutron energies (E_i) of 8, 20, and 50 meV were used on MARI selected via a Gd-Fermi chopper. The μSR measurement was carried out on the MUSR spectrometer with the detectors in a longitudinal configuration. The powdered sample was mounted on a high purity silver plate using diluted GE varnish and covered with kapton film which was cooled down to 1.2 K in a standard ^{4}He cryostat with He-exchange gas. Spin-polarized muon pulses were implanted into the sample and positrons from the resulting decay were collected in positions either forward or backwards of the initial muon spin direction. The asymmetry is calculated by $G_z(t) = [N_F(t) - \alpha N_B(t)]/[N_F(t) + \alpha N_B(t)]$, where $N_B(t)$ and $N_F(t)$ are the number of counts at the detectors in the forward and backward positions and α is a constant determined from calibration measurements made in the paramagnetic state with a small (20 G) applied transverse magnetic field.

III. RESULTS AND DISCUSSION

A. Room-temperature neutron diffraction

Powder neutron diffraction measurements were carried out at room temperature on the polycrystalline $RNiC_2$ (R = Ce and La) samples. Rietveld refinement was carried out using the GSAS software on the basis of an orthorhombic $CeNiC_2$-type crystal structure (space group No. 38) [17]. In this structure the Ce/La atom occupies $2a$ sites, the Ni atom $2b$ sites, and the C atom $4e$ sites. The Rietveld refinement profile along with neutron diffraction patterns of these compounds are shown in Figs. 1(b) and 1(c). One small impurity peak was detectable in $CeNiC_2$ (the height of strongest impurity peak is about 1% of the intensity of the maximum sample peak) while none were observed in $LaNiC_2$, indicating that the samples are single phase. The site occupancies were all fixed at 100%. The results of the refinements are displayed in Table I. Observed lattice parameters are in agreement with the previously reported values [17]. The nearest-neighbor distances are 3.8305 Å for Ce-Ce, 3.0671 Å for Ce-Ni, and 1.9687 Å for Ni-C.

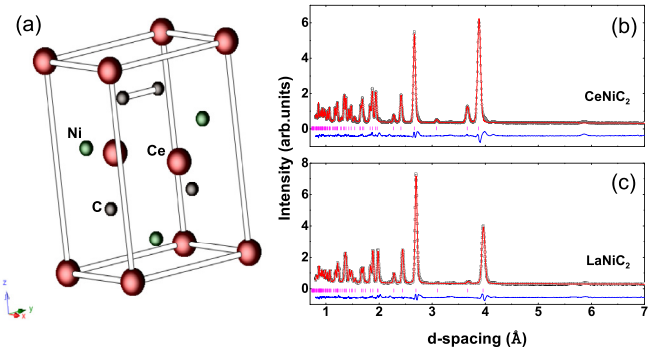

FIG. 1. (Color online) (a) The orthorhombic crystal structure of $CeNiC_2$ where the Ce atoms are in red, the Ni atoms are in green, and the C atoms are in black. (b) and (c) show the Rietveld refinements of the neutron powder diffraction patterns of $CeNiC_2$ and $LaNiC_2$ at 300 K. The data are shown as black circles, and the result of the refinement as solid lines (red).

B. Magnetization and heat capacity

The temperature (T) variation of the dc magnetic susceptibility ($\chi = M/H$, where H is the applied magnetic field) measured in a zero-field-cooled condition in $H = 40$ kOe is shown in Fig. 2(a). χ shows a drop below 20 K with decreasing T. This corresponds to the PM/AFM transition (T_{N_1}) in the sample. The magnetic susceptibility of $CeNiC_2$

TABLE I. A summary of the results obtained from the refinement of the room-temperature neutron powder diffraction data: the lattice parameters and atomic positions. The site occupancy for all the atoms was fixed to 100%. The reliability factors (weighted profile factor $R_{wp} = 5\%$) were calculated by comparing the fit to the data (space group No. 38, *Amm*2).

		a (Å)	b (Å)	c (Å)
$CeNiC_2$		3.876(2)	4.548(2)	6.161(1)
$LaNiC_2$		3.957(2)	4.561(1)	6.199(2)
Atom	Site	x	y	z
Ce	$2a$	0.00	0.00	1.00
Ni	$2b$	0.500	0.00	0.6138(2)
C	$4e$	0.500	0.3509(2)	0.8043(1)
La	$2a$	0.00	0.00	1.00
Ni	$2b$	0.500	0.00	0.6137(1)
C	$4e$	0.500	0.3513(1)	0.8047(2)

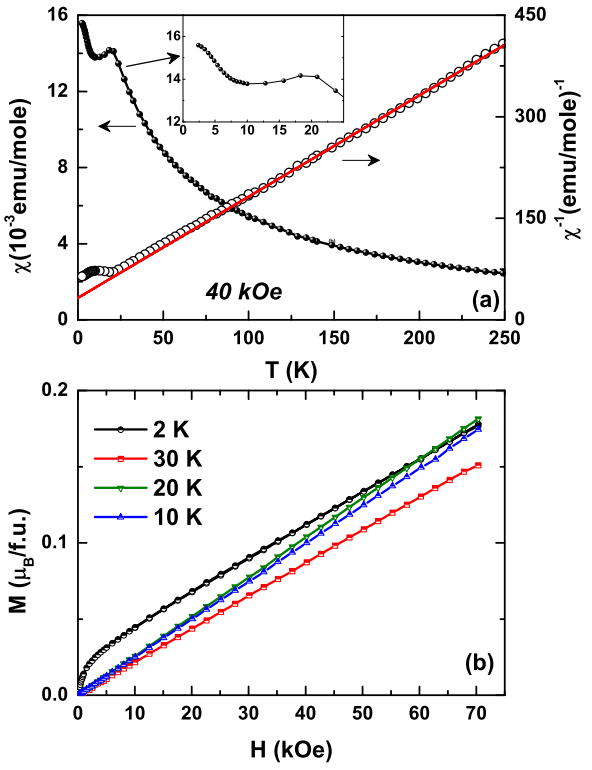

FIG. 2. (Color online) (a) Temperature dependence of the magnetic susceptibility [$\chi(T)$] and the inverse $\chi(T)$ of polycrystalline $CeNiC_2$. The straight lines show fits to CW behavior in the high-temperature region. The inset shows $\chi(T)$ between 2 and 25 K. (b) Isothermal field dependence of magnetization at different constant temperatures.

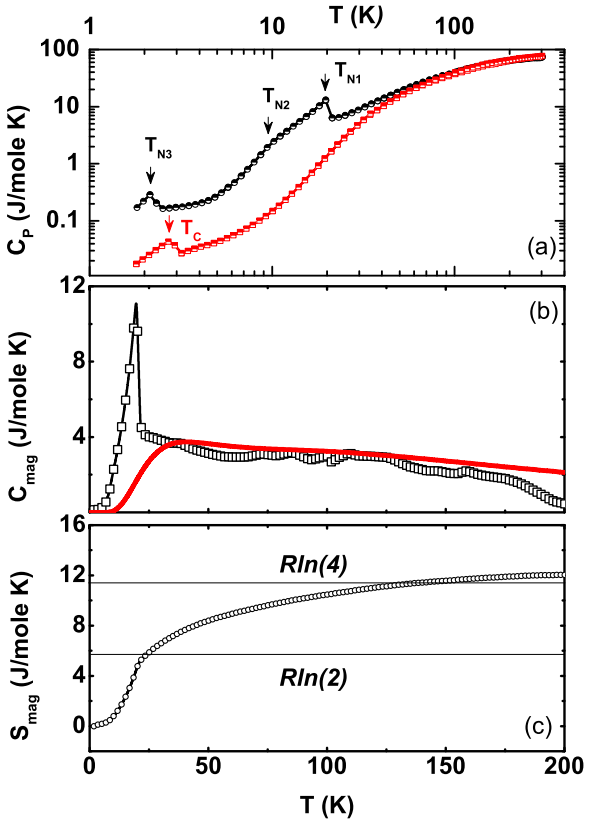

FIG. 3. (Color online) (a) Temperature dependence of the heat capacity of $CeNiC_2$ (black circle) and the phonon reference compound $LaNiC_2$ (red square). (b) Estimated magnetic contribution of the heat capacity plotted as C_{mag} vs T, and the red curve represents the crystal electric field contribution to specific heat according to the crystal field level scheme deduced from the inelastic neutron scattering data. (c) The temperature-dependent magnetic entropy estimated from the experimental data in (b).

above 50 K exhibits Curie-Weiss (CW) behavior. A linear least-squares fit yields an effective magnetic moment $p_{\text{eff}} = 2.30\mu_B$, which is close to free Ce^{3+}-ion value ($2.54\mu_B$), and a negative paramagnetic Curie temperature $\theta_p = -15$ K. The value of the magnetic moment suggests that the Ce atoms are in their normal Ce^{3+} valence state, which agrees with a smooth variation of the unit cell volume in the $RNiC_2$ series [17]. A negative value of θ_p is indicative of a negative exchange constant and AFM ordering. $LaNiC_2$ shows weak Pauli paramagnetism-type behavior (not shown here, which confirms that Ni is nonmagnetic in the $RNiC_2$ series) [18].

Figure 2(b) shows the M vs H isotherms recorded at different temperatures. $M-H$ data imply that the net magnetization in the ordered state of $CeNiC_2$ is extremely low. It is far from saturation and barely reaches 7% of that expected theoretically, $gJ = 2.14\mu_B$ for Ce^{3+} ions, in a 70 kOe magnetic field. This is consistent with previously reported results [10,11]. The low values of the observed magnetization is expected for an AFM ground state due to the cancellation of magnetization from different magnetic sublattices of Ce ions.

Zero-field C_P vs T data of both compounds from 2 to 300 K are shown in Fig. 3(a). For $LaNiC_2$, $C_P(T)$ data show a sharp discontinuity between 2 and 3 K, which is consistent with the transition to the superconducting state. The discontinuity in the heat capacity of $LaNiC_2$, $\Delta C/\gamma T_C = 1.20$, suggests weak electron-electron coupling and confirms the bulk nature of superconductivity [18]. For $CeNiC_2$ a clear signature of anomaly is observed at $T_{N_1} = 19.5$ K and $T_{N_3} = 2.5$ K and a further weak anomaly is observed at $T_{N_2} = 10$ K, which matches well with previous reports [18]. We have carefully looked at the low T behavior of C_P. At $T \ll \Theta_D$ (Θ_D is the Debye temperature), the lattice part of the heat capacity C_{Debye} has a T^3 dependence. We estimate γ and Θ_D using the same method as reported by Pecharsky *et al.* [18] and find similar values of γ (6.0 mJ mol^{-1} K^{-2}) and Θ_D (380 K).

The magnetic contribution to the specific heat C_{mag} is shown in Fig. 3(b). The C_{mag} was estimated by subtracting off the lattice contribution equal to the specific heat of isostructural $LaNiC_2$. It is to be noted that below 3 K, $LaNiC_2$ shows a superconducting transition, hence it is not ideal as a phonon reference below 3 K. However, considering the difference in the heat capacity of $CeNiC_2$ and $LaNiC_2$ (which is very small below 3 K), our analysis to estimate the magnetic contribution using $LaNiC_2$ as a phonon reference will not change our interpretation of the data. The effect of a crystal electric field is reflected as a broad Schottky-type anomaly centered around 52 K in C_{mag}. The solid curve in Fig. 3(b) represents the crystal field contribution to specific heat according to the CEF level scheme obtained from the analysis of inelastic neutron scattering data. The magnetic contribution to entropy S_{mag} was

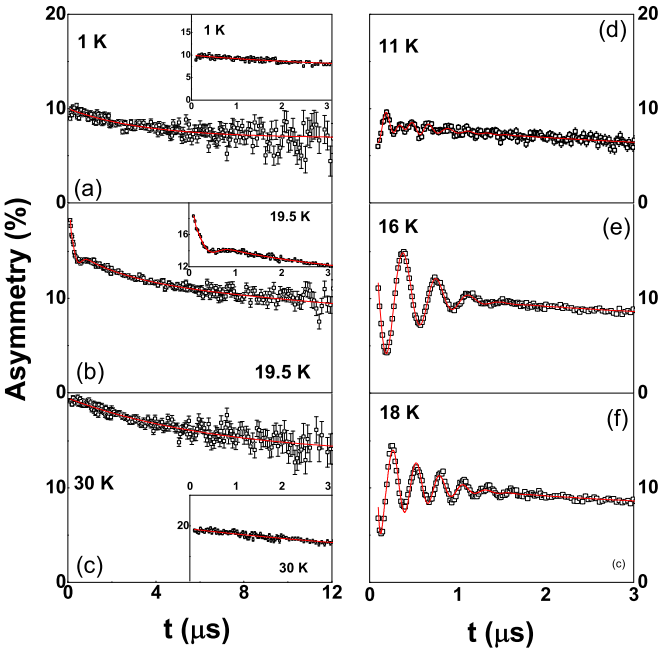

FIG. 4. (Color online) Zero-field μSR spectra plotted as asymmetry vs time at various temperatures of $CeNiC_2$. The solid lines depict fits using Eq. (1) (see text). The insets of (a)–(c) show the zero-field spectra in the low time domain.

obtained by integrating the $C_{\rm mag}(T)/T$ vs T plot and is shown in Fig. 3(c). The value of $S_{\rm mag}$ around the magnetic ordering temperature is comparable with $R\ln 2$, suggesting a CEF split doublet ground state in $CeNiC_2$, and is confirmed by the INS data in Sec. III D.

C. Muon spin relaxation

The time dependence of asymmetry (μSR) spectra of $CeNiC_2$ measured at various temperatures in zero field are shown in Figs. 4(a)–4(f). The insets of Figs. 4(a)–4(c) show the zero-field spectra in the low time domain. The spectra show an exponential-type decay above 20 K in the paramagnetic state. In the temperature range 10 K $\leqslant T \leqslant$ 20 K, muon spin precession with two frequencies is observed, indicating that at least two muon sites exist in the compound. Below 10 K, as shown in Fig. 4(a), muon spin precession is not observable due to the fact that internal fields exceed the maximum internal field detectable on the μSR spectrometer due to the pulse width of the ISIS muon beam. In the temperature ranges 2 K $\leqslant T \leqslant$ 10 K and 20 K $\leqslant T \leqslant$ 30 K, we used a simple exponential decay plus constant background to fit our μSR spectra. In the range 10 K $\leqslant T \leqslant$ 20 K, the spectra were fitted with [19,20]

$$G_z(t) = \sum_{i=1}^{n} A_i \cos(\gamma_\mu H_i t + \phi) e^{-\frac{\sigma_i^2 t^2}{2}} + A_3 e^{-\lambda t} + A_{\rm bg}, \quad (1)$$

where the initial amplitude of the exponential decay and the oscillatory component are A_3 and A_i, respectively, the internal magnetic fields at the muon stopping site i are H_i, the Gaussian decay rate is σ_i, λ is the muon depolarization rate, ϕ is the common phase, $\gamma_\mu/2\pi = 135.53$ MHz T^{-1},

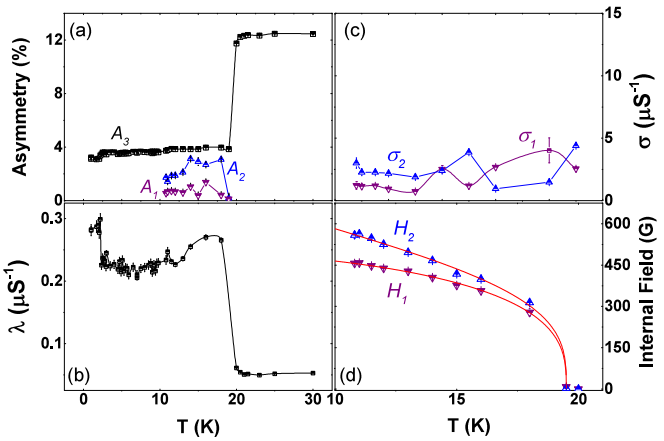

FIG. 5. (Color online) The temperature dependence of (a) the initial asymmetries A_1, A_2, and A_3, (b) the depolarization rate λ, (c) the depolarization rates σ_1 and σ_2, and (d) the internal fields H_1 and H_2. The solid line in (d) is a fit to Eq. (2) (see text).

and $A_{\rm bg}$ is the background. The temperature dependences of these parameters are shown in Figs. 5(a)–5(d). At 20 K, as shown in Fig. 5(a), there is a loss of 2/3 of the value of the initial asymmetry (1/3 is left) of A_3 from the high-temperature value. The initial asymmetry associated with frequency terms A_1 and A_2 starts to increase below this temperature (20 K) [see Fig. 5(a)], indicating the presence of a long-range ordered state in $CeNiC_2$ which agrees with the specific heat, magnetic susceptibility, and neutron diffraction data [9–12,18]. The temperature dependence of the exponential decay term is shown in Fig. 5(b). The muon depolarization rate (λ) was found to suddenly increase at T_{N_1}, indicating a transition between the paramagnetic and ordered states. However, λ shows a weak anomaly at T_{N_2} and T_{N_3}, where there is a rearrangement of the spins and a change in the magnetic structure which is in agreement with the reported change in the propagation vector from the neutron diffraction study [10]. Figure 5(c) shows the temperature dependence of the muon depolarization rate. σ_1 and σ_2 remain almost constant within the temperature range 10 K $\leqslant T \leqslant$ 20 K.

In order to find out the nature of the magnetic interaction in $CeNiC_2$, the temperature dependence of both internal fields (H_1 and H_2) was fitted:

$$H_i(T) = H_0\left[1 - \left(\frac{T}{T_N}\right)^{\alpha_i}\right]^{\beta_i}. \quad (2)$$

The observed parameters are β_1 and $\beta_2 = 0.34(2)$ and $0.31(2)$, $H_0 = 508$ and 600 G, α_1 and $\alpha_2 = 3.12$ and 1.234, and $T_N = 19.5(3)$ K [see Fig. 5(d)]. A good fit with $\beta \sim 0.31$ (or 0.34) suggests the magnetic interactions in $CeNiC_2$ constitute a three-dimensional (3D) Ising spin system with long-range spin-spin interactions. $\alpha > 1$ indicates complex magnetic interactions in this system [21,22].

We also recorded the field-dependent asymmetry spectra at 1.2 K and fitted them using an exponential function plus constant background [see Fig. 6(a)]. The initial asymmetry (A_3) and depolarization term (λ) as a function of applied longitudinal field at 1.2 K is shown in Figs. 6(b) and 6(c). We used two different models for the field dependence of

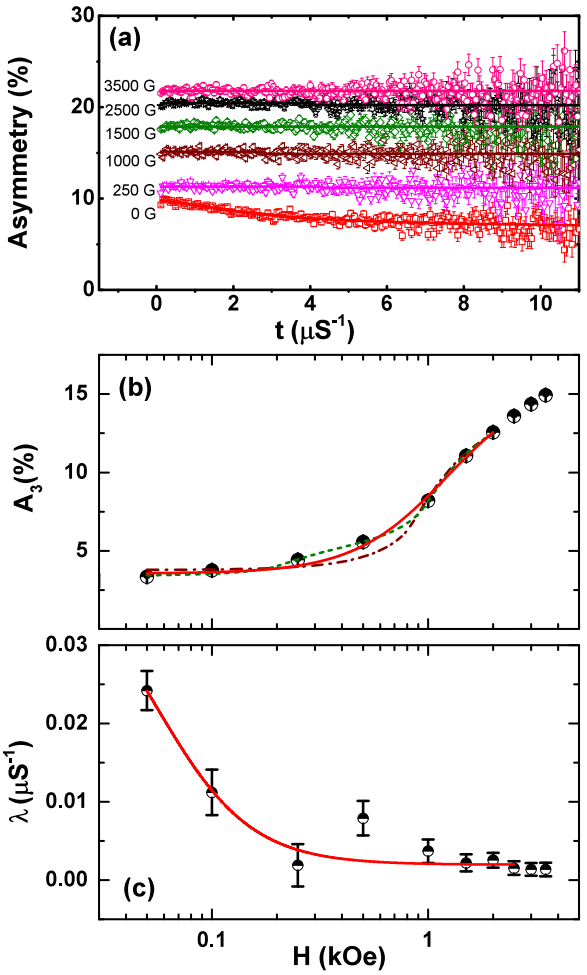

FIG. 6. (Color online) (a) Field-dependent μSR spectra at 1.2 K. (b) The longitudinal component of the initial asymmetry (A_3). The solid and dashed-dotted lines represent fits to Eq. (3), while the dotted line represents fits to Eq. (4). (c) The depolarization rate (λ) at 1.2 K. The solid line represents the fit to Eq. (5). It is to be noted that in our analysis we have used one value of α (=0.956 00) estimated in a transverse field of 20 G well above T_N. Further, it is to be noted that we have used the data between 0 and 2000 G in fitting to avoid the error due to the change in the α between 2500 and 3500 G.

A_3 to compare with the data: (i) a single characteristic field H_0 [23],

$$A_3(H) = f_0 + F\left[\frac{3}{4} - \frac{1}{4b^2} + \frac{(b^2-1)^2}{8b^3}\ln\left|\frac{(b+1)}{(b-1)}\right|\right], \quad (3)$$

where f_0 is the constant offset and F is the scaling factor, while $b = H/H_0$ (H_0 is the internal field) [a detailed discussion of Eq. (3) is given in Ref. [23]], and (ii) used a quadratic-type decoupling function [23],

$$A_3(H) = f_0 + F\frac{b^2}{1+b^2}. \quad (4)$$

The fits were made using Eqs. (3) and (4) and an internal field of 1223(20) and 1227(40) G [shown by the dashed-dotted line in Fig. 6(b)] was obtained, respectively. The larger value of the internal field observed at 1.2 K compared to that estimated between 10 and 20 K again indicates different magnetic structures at 1.2 K and between 10 and 20 K. As we detect the presence of two frequencies between 10 and 19.5 K, we have also tried to fit the field-dependent asymmetry data using two internal fields in Eq. (3), i.e., adding a second term. This shows very good agreement with the data, shown by the solid line in Fig. 6(b). The values of the internal fields at two muon sites obtained are 1215(10) and 380(5) G. This supports the presence of two muon stopping sites in $CeNiC_2$.

The relaxation rate decreases with applied field, as is conventionally expected, and we fitted the field dependence using a modified version of Redfield's equation [24],

$$\lambda = \lambda_0 + \frac{2\gamma_\mu^2\Delta^2\tau_C}{1+\gamma_\mu^2H^2\tau_C}, \quad (5)$$

where γ_μ is the muon gyromagnetic ratio, Δ describes the width of the field distribution, and τ is the characteristic time scale for the spin fluctuations experienced by the muons. The fit of $\lambda(H)$ data by Eq. (5) is shown by the solid red curve in Fig. 6(c). A good fit is obtained for $\lambda_0 = 0.0015\ \mu s^{-1}$, $\Delta = 3.7$ G, and $\tau_C = 15 \times 10^{-8}$ s. The observed value of τ_C in $CeNiC_2$ is comparable with that observed in $CePd_{0.15}Rh_{0.85}$ [25].

D. Inelastic neutron scattering

In order to understand the origin of the reduced moment magnetism and also to investigate crystal field excitations and their energy level scheme in $CeNiC_2$, we have performed an inelastic neutron scattering study. Neutrons with incident energies $E_i = 8$, 20, and 50 meV were used to record the INS spectra at 5, 25, 50, and 100 K for scattering angles between 3° and 135°. The INS measurements were carried out on the polycrystalline samples of $CeNiC_2$ and $LaNiC_2$ using the MARI spectrometer. The data of $LaNiC_2$ were used to subtract the phonon contribution in $CeNiC_2$.

For magnetic neutron scattering the partial differential cross section, which measures the probability of scattering per solid angle per unit energy, is [26]

$$\frac{d^2\sigma}{d\Omega dE'} = \frac{k'}{k}\frac{N}{\hbar}(\gamma r_0)^2F(Q)^2\sum_{\alpha\beta}(\delta_{\alpha\beta} - \widehat{Q}_\alpha\widehat{Q}_\beta)S^{\alpha\beta}(Q,\omega), \quad (6)$$

where k' and k are the scattered and incident neutron wave vectors, $\gamma r_0 = 5.391$ fm is the magnetic scattering length, Q is the momentum transfer, $F(Q)$ is the magnetic form factor, ω is the energy transfer, N is the number of moments, and the summation runs over the Cartesian directions. The magnetic scattering function $S^{\alpha\beta}(Q,\omega)$ is proportional to the space and time Fourier transform of the spin-spin correlation function [26].

To determine the correct magnetic contribution to the measured spectra, we have subtracted the phonon contribution using the data of the nonmagnetic reference compound. We first used a direct subtraction method [$S(Q,\omega)_{CeNiC_2} - S(Q,\omega)_{LaNiC_2}$] and later allowed for a difference in the total scattering cross section, [$S(Q,\omega)_{CeNiC_2} - \sigma_c \times S(Q,\omega)_{LaNiC_2}$] (where $\sigma_c = 0.8288$ is the ratio of the total scattering cross section of $CeNiC_2$ and $LaNiC_2$) [27,28]. Both analyses gave a similar magnetic response. But the second method gave a slightly

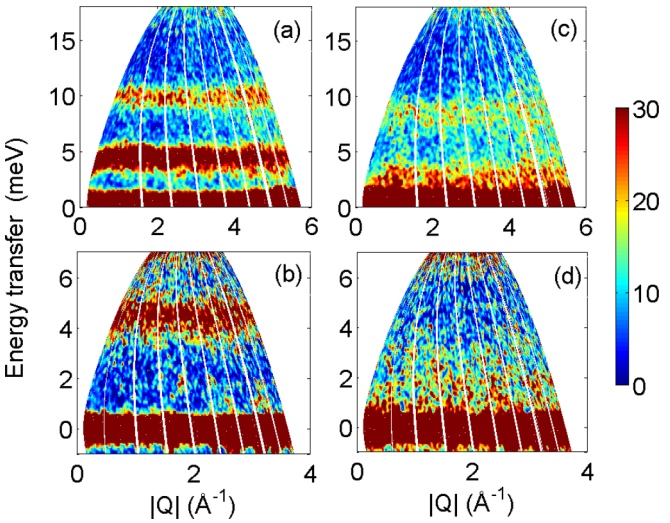

FIG. 7. (Color online) Contour plots of the inelastic scattering intensity (in mb/sr meV f.u.) plotted as energy transfer vs wave vector transfer (Q) of $CeNiC_2$ measured with $E_i = 20$ meV [(a) and (c)] and 8 meV [(b) and (d)] at 5 and 25 K, respectively.

better estimation at the low energy side in subtracting the nuclear elastic peak at zero energy transfer, and hence in this paper we present all our data analyzed using the second method.

Figures 7(a)–7(d) display the color-coded plot of the scattering intensity of the energy versus momentum transfer of $CeNiC_2$. Two inelastic excitations at 8 and 30 meV (see Fig. 8) were observed with a significant intensity at low scattering vectors at 25 K. The absence of these excitations in $LaNiC_2$ indicates they are magnetic in origin. The 5 K data have an additional magnetic excitation with a maximum at around 4.5 meV. This excitation is not present at 25 K, as shown in Figs. 7(b)–7(d), where the elastic line is broadened, signifying the presence of a spin wave below magnetic ordering. In the paramagnetic state, the spectral weight is shifted towards the elastic line, and quasielastic scattering (QES) is observed. Figures 8(a)–8(c) reveal the color-coded contour map of the magnetic scattering of $CeNiC_2$ at 5 K estimated by subtracting the data of $LaNiC_2$ (using the second method) measured with incident energies $E_i = 50$ meV [Fig. 8(a)], 20 meV [Fig. 8(b)], and 8 meV [Fig. 8(c)], respectively.

Figures 9(a) and 9(b) represent the Q-dependent energy integrated intensity between (i) 5.85 and 11.05 meV and (ii) 22 and 35 meV at 25 K of $CeNiC_2$ for incident energy $E_i = 20$ and 50 meV, respectively. It follows the square of the Ce^{3+} magnetic form factor [$F^2(Q)$], which suggests that the inelastic excitations result mainly from single-ion CEF transitions. The scattering at the highest Q (not shown here) is comparable for $CeNiC_2$ and $LaNiC_2$, which indicates similar phonon contributions in these compounds. At low Q, the magnetic scattering is strong and with a small phonon contribution in $CeNiC_2$. This can be seen clearly in the 1D cuts made from the 2D color plots at low Q from 0 to 4 Å^{-1} (see Fig. 10) at 5, 25, and 100 K.

In order to estimate the quasielastic linewidth we have analyzed the 8 meV data using a Lorentzian function. We used an elastic line resolution function and an additional Lorentzian

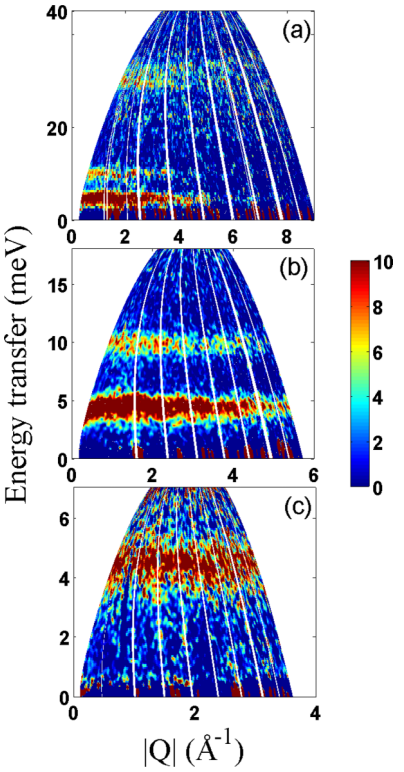

FIG. 8. (Color online) The color-coded contour map of the magnetic scattering of $CeNiC_2$ at 5 K estimated by subtracting (see text) the data of $LaNiC_2$ measured with incident energy E_i = (a) 50, (b) 20, and (c) 8 meV, respectively.

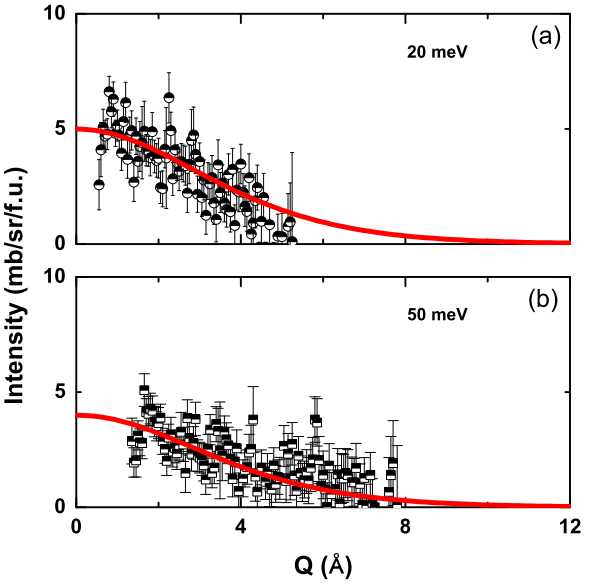

FIG. 9. (Color online) The Q dependence of total energy integrated intensity between (a) 5.85 and 11.05 meV and (b) 22 and 35 meV at 25 K for incident energy $E_i = 20$ and 50 meV, respectively. The solid line represents the square of the Ce^{3+} magnetic form factor (scaled to match with the data).

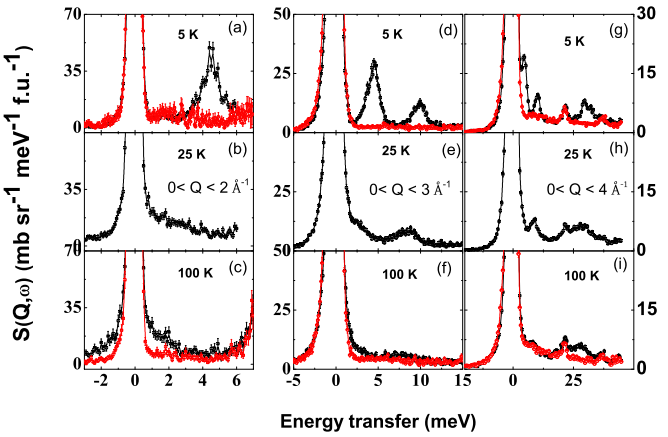

FIG. 10. (Color online) The Q-integrated 1D cuts of the total scattering from $CeNiC_2$ (black square) and $LaNiC_2$ (red circle) with an incident energy $E_i = 8$ meV (left panel), 20 meV (middle panel), and 50 meV (right panel), respectively.

function to model the quasielastic component to fit our data. The widths of the elastic component were fixed from the measurements of vanadium with the same incident energy and frequency of the Fermi chopper. Figure 11 (left y axis) shows the T dependence of the half width at half maximum (HWHM, Γ). Γ does not change much with temperature. An estimate of the Kondo temperature (T_K) can be obtained from the value of Γ at 0 K (we used a Γ value in between 50 and 80 K). For $CeNiC_2$, the Γ value gives an estimation of $T_K = 11$ K. However, at lower temperatures (around 25 K) a slightly higher Γ value was observed. We attribute this to the presence of short-range magnetic correlations just above T_{N_1}.

We now proceed with a more detailed analysis of the observed CEF excitations. In the orthorhombic point symmetry, $Amm2$ (C_{2v}), at the Ce^{3+} site and taking the z axis as the quantization axis (i.e., $x \| a$, $y \| b$, and $z \| c$), the CEF

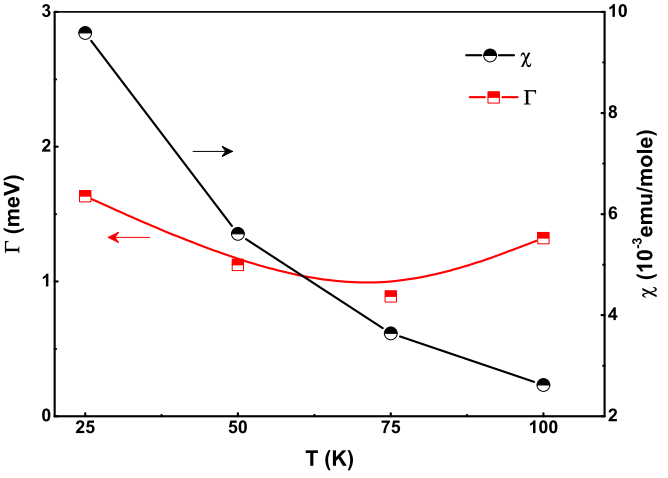

FIG. 11. (Color online) Temperature dependence of the quasielastic linewidth (left y axis) and susceptibility (right y axis) obtained from fitting INS data measured with an incident energy of 8 meV.

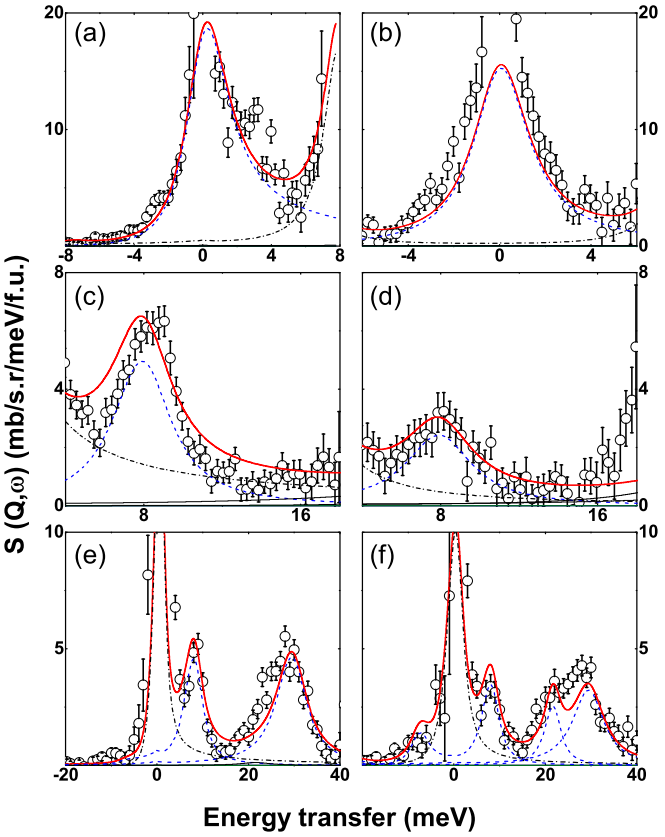

FIG. 12. (Color online) The estimated magnetic scattering of $CeNiC_2$ at 25 K (left panel) and 100 K (right panel) for momentum transfer $|Q|$ from 0 to 2 Å^{-1} for 8 meV, $|Q|$ from 0 to 3 Å^{-1} for 20 meV, and $|Q|$ from 0 to 4 Å^{-1} for 50 meV. The solid lines are the fits based on the crystal electric field model and the dashed and dashed-dotted lines are the components of the fit.

Hamiltonian can be represented as follows:

$$H_{\mathrm{CEF}} = B_2^0 O_2^0 + B_2^2 O_2^2 + B_4^0 O_4^0 + B_4^2 O_4^2 + B_4^4 O_4^4, \quad (7)$$

where O_n^m are the Stevens operators and B_n^m are the CEF parameters to be determined from the experimental data of inelastic neutron scattering [29,30]. The value of B_2^0 and B_2^2 can be accurately determined using the high-temperature expansion of the magnetic susceptibility [31,32], which gives B_2^0 and B_2^2 in terms of the CW temperatures, θ_a and θ_b for an applied field parallel to the a axis and b axis, respectively, and B_2^0 in terms of θ_c for an applied field parallel to the c axis. The detailed formulation has been given in Ref. [9]. From their formula we have determined the values of $B_2^0 = 0.085\,31$ meV and $B_2^2 = -0.8913$ meV. It is to be noted that these values are valid for an isotropic exchange interaction. They were kept fixed in our initial analysis of the INS data which did not give a good fit to the data and then finally we allowed to vary all five CEF parameters independently.

The solid lines in Figs. 12(a)–12(f) represent the fit to the CEF model for simultaneous refinement of all six data sets for 8, 20, and 50 meV incident energies (we first refined the 25 and 100 K data). The phenomenological crystal field parameters B_n^m obtained from the best fit are given in Table II.

TABLE II. CEF parameters B_n^m, molecular field parameters ($\lambda_\xi, \xi = a,b,c$), and temperature-independent constant susceptibility (χ_ξ). The parameters were estimated by a simultaneous fit to the INS data at 25 and 100 K and then fitting the single-crystal susceptibility.

	25 and 100 K
B_2^0 (meV)	0.080(2)
B_2^2 (meV)	−0.650(1)
B_4^0 (meV)	−0.086(2)
B_4^2 (meV)	−0.050(3)
B_4^4 (meV)	0.209(2)
λ_a (mol/emu)	3.856
λ_b (mol/emu)	−51.214
λ_c (mol/emu)	−7.234
χ_a ($\times 10^{-3}$ emu/mol)	2.505
χ_b ($\times 10^{-3}$ emu/mol)	2.626
χ_c ($\times 10^{-3}$ emu/mol)	2.642

The CEF wave functions obtained from the simultaneous fit to 25 and 100 K, INS data are given by

$$|\psi_1^{\pm}\rangle = 0.4104\left|\pm\tfrac{5}{2}\right\rangle + 0.9115\left|\pm\tfrac{1}{2}\right\rangle - 0.0273\left|\pm\tfrac{3}{2}\right\rangle, \quad (8)$$

$$|\psi_2^{\pm}\rangle = 0.8719\left|\pm\tfrac{5}{2}\right\rangle - 0.4010\left|\pm\tfrac{1}{2}\right\rangle - 0.2812\left|\pm\tfrac{3}{2}\right\rangle, \quad (9)$$

$$|\psi_3^{\pm}\rangle = 0.2672\left|\pm\tfrac{5}{2}\right\rangle - 0.0916\left|\pm\tfrac{1}{2}\right\rangle + 0.9593\left|\pm\tfrac{3}{2}\right\rangle. \quad (10)$$

ψ_1 is the ground state (GS) wave function, whereas ψ_2 is for the first excited state at 92 K and ψ_3 is for the second excited state at 342 K above the GS. The GS magnetic moments of the Ce atoms $\langle\mu_x\rangle$, $\langle\mu_y\rangle$, and $\langle\mu_z\rangle$, along the three crystallographic axes a, b, and c, respectively, can be calculated from

$$\langle\mu_z\rangle = \langle\psi_1^{\pm}|g_J J_z|\psi_1^{\pm}\rangle, \quad (11)$$

$$\langle\mu_x\rangle = \langle\psi_1^{\pm}|\frac{g_J}{2}(J^+ + J^-)|\psi_1^{\pm}\rangle, \quad (12)$$

$$\langle\mu_y\rangle = \langle\psi_1^{\pm}|\frac{g_J}{2i}(J^+ - J^-)|\psi_1^{\pm}\rangle. \quad (13)$$

The calculated magnetic moments in the presence of an applied magnetic field ($H = 10$ kOe; $T = 1$ K) using the GS wave function are $\langle\mu_x\rangle = 0.583\mu_B$, $\langle\mu_y\rangle = 0.6876\mu_B$, and $\langle\mu_z\rangle = 0.341\mu_B$. This is in agreement with neutron diffraction data, which give a possible direction of moment along the b axis [10]. However, it is to be noted that the neutron diffraction study was unable to find an accurate direction and magnitude of the moment due to the limited numbers of the magnetic Bragg reflections [10].

After obtaining CEF parameters from the simultaneous fit of the six INS data sets at 25 and 100 K, we have analyzed 20 meV INS data at 5 K (i.e., below the magnetic ordering) adding the molecular field term in the Hamiltonian. We kept the values of CEF parameters (which were obtained from 25 and 100 K as mentioned above) fixed for the analysis of 5 K data and varied molecular fields. First we varied only the molecular field along the x axis (H_x) while keeping zero-molecular fields along the b (H_y) and c axes (H_z). This method did not give a good fit to the data. Then we tried to vary H_y (while keeping $H_x = 0$ and $H_z = 0$), however, we did not obtain a good fit for this method either. Hence finally we varied H_x and H_y simultaneously (keeping $H_z = 0$), which gave a reasonably good fit to the data (it is to be noted that when we also allowed to vary H_z it gave almost a zero value). The values of the molecular field estimated from the analysis are $H_x = 79.3(1.8)$ T and $H_y = 76.5(1.7)$ T. The quality of the fit can be seen in Fig. 13(a). The presence of molecular fields along the a and b axes may suggest that the Ce moment is confined to the ab plane and not along the a or b axis. A detail neutron diffraction investigation using a high neutron flux instrument on a $CeNiC_2$ single crystal will be helpful to understand the presence of the molecular field along the a and b axes. To check the reliability of our set of CEF parameters we model the single-crystal magnetic susceptibility data from literature [9]. The observed anisotropic magnetic susceptibility data correctly fit with our calculated $\chi(T)$ using CEF parameters [see Fig. 13(b)].

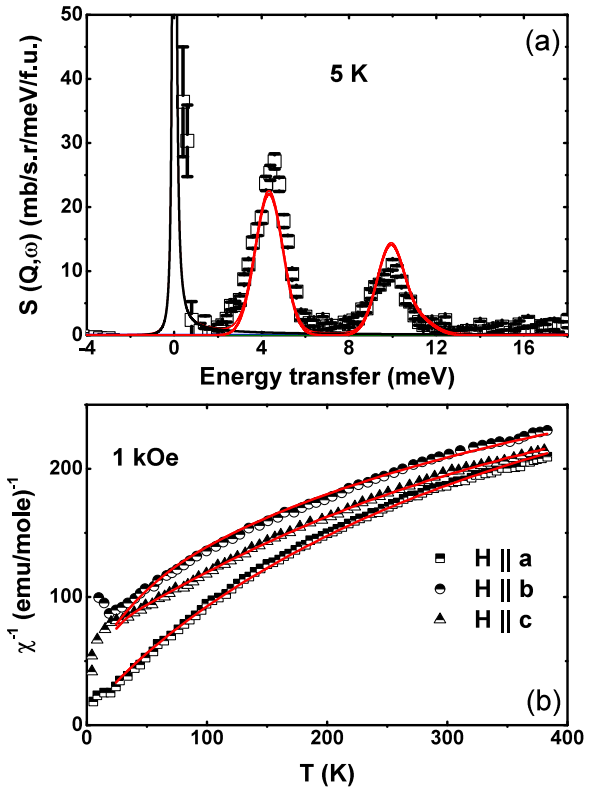

FIG. 13. (Color online) (a) The estimated magnetic scattering of $CeNiC_2$ at 5 K with $E_i = 20$ meV. The solid line represents the fit using CEF and the molecular field (see text). (b) Temperature dependence of the inverse susceptibilities along the three crystallographic axes of $CeNiC_2$. The solid line represents the fit based on the CEF model.

IV. CONCLUSIONS

We have studied the magnetic properties of $CeNiC_2$ using magnetic susceptibility, heat capacity, inelastic neutron scattering, and μSR measurements. A magnetic transition around 20 K is observed with the emergence of oscillations in zero-field μSR spectra. We fitted the temperature dependence of

the internal magnetic fields to a model of a mean field magnet, which revealed the 3D nature of the magnetic interactions.

INS measurements of polycrystalline $CeNiC_2$ at low temperatures (above 20 K) indicate two CEF excitations at 8 and 30 meV. At 5 K, we observe an additional peak at 4.5 meV due to spin-wave excitations. Above T_N, this peak is not present, but quasielastic scattering is observed. A linear fit to the temperature dependence of the quasielastic linewidth gives an estimate of $T_K = 11$ K. From an analysis of INS and magnetic susceptibility data with a CEF model, we propose a CEF scheme for $CeNiC_2$. The CEF scheme correctly predicts the direction of the ordered moment, but the estimated magnetic moment at 2 K is $0.6876\mu_B$/Ce, which is higher compared to the moment as observed from neutron diffraction ($0.25\mu_B$/Ce). We believe that the observed reduced moment in the neutron diffraction study is due to the presence of hybridization between the localized Ce^{3+} f electrons and the conduction band. It is to be noted that in our CEF analysis we have used only a single-ion effect and have not included Kondo interactions, which are responsible for the observed reduction of the Ce moment. A very similar effect has also been observed in $CeRu_2Al_{10}$ [33,34] and in $CeCoGe_3$ [19]. Further, the susceptibility analysis reveals anisotropic molecular fields, stronger along the b axis, which are also in agreement with the direction of the moment along the b axis. The spin-wave measurements on a $CeNiC_2$ single crystal will help to shed more light on the anisotropic exchange interactions in $CeNiC_2$.

We note furthermore that the estimated on-site Kondo exchange (11 K) is of the same order of magnitude as the magnetic phase transition temperatures, which classifies this compound as a magnetically ordered Kondo lattice. The complexity of spin ordering in $CeNiC_2$ is inferred as a consequence of admixing of crystal electric field energies together with Kondo and RKKY exchanges, and we believe that our study and determination of the CEF parameters presented in this work establish the essential ingredients with which to formulate an understanding of the ground state in $CeNiC_2$.

ACKNOWLEDGMENTS

A.B. thanks the FRC of JU, NRF of South Africa and ISIS-STFC for funding support. D.T.A. and A.D.H. would like to thank CMPC-STFC, Grant No. CMPC-09108, for financial support. A.M.S. thanks the SA-NRF (Grant No. 78832) and the UJ Research Committee for financial support.

[1] A. Georges, G. Kotliar, W. Krauth, and M. J. Rozenberg, Rev. Mod. Phys. **68**, 13 (1996).
[2] C. M. Varma, Rev. Mod. Phys. **48**, 219 (1976).
[3] P. Coleman, in *Handbook of Magnetism and Advanced Magnetic Materials*, edited by H. Knoemuller and S. Parkin (Wiley, New York, 2007), Vol. 1, p. 95.
[4] P. S. Riseborough, Adv. Phys. **49**, 257 (2000); Phys. Rev. B **45**, 13984 (1992).
[5] G. R. Stewart, Rev. Mod. Phys. **73**, 797 (2001); A. Amato, *ibid.* **69**, 1119 (1997).
[6] H. v. Löhneysen, A. Rosch, M. Vojta, and P. Woelfle, Rev. Mod. Phys. **79**, 1015 (2007).
[7] A. M. Strydom, Physica B **404**, 2981 (2009).
[8] D. T. Adroja, A. D. Hillier, Y. Muro, T. Takabatake, A. M. Strydom, A. Bhattacharyya, A. Daoud-Aladine, and J. W. Taylor, Phys. Scr. **88**, 068505 (2013).
[9] H. Onodera, Y. Koshikawa, and M. Kosaka, J. Magn. Magn. Mater. **182**, 161 (1998).
[10] K. Motoya, K. Nakaguchi, N. Kayama, K. Inari, J. Akimitsu, K. Izawa, and T. Fujita, J. Phys. Soc. Jpn. **66**, 1124 (1997).
[11] W. Schäfer, G. Will, J. K. Yakinthos, and P. A. Kotsanidis, J. Alloys Compd. **180**, 251 (1992).
[12] M. Murase, A. Tobo, H. Onodera, Y. Hirano, T. Hosaka, S. Shimomura, and N. Wakabayashi, J. Phys. Soc. Jpn. **73**, 2790 (2004).
[13] W. H. Lee, H. K. Zeng, Y. D. Yao, and Y. Y. Chen, Physica C **266**, 138 (1996).
[14] A. D. Hillier, J. Quintanilla, and R. Cywinski, Phys. Rev. Lett. **102**, 117007 (2009).
[15] S. Shimomura, C. Hayashi, G. Asaka, N. Wakabayashi, M. Mizumaki, and H. Onodera, Phys. Rev. Lett. **102**, 076404 (2009).
[16] J. Laverock, T. D. Haynes, C. Utfeld, and S. B. Dugdale, Phys. Rev. B **80**, 125111 (2009).
[17] P. Kotsanidis, J. K. Yakinthos, and E. Gamari-Seale, J. Less Common Met. **152**, 287 (1989).
[18] V. K. Pecharsky, L. L. Miller, and K. A. Gschneidner, Jr., Phys. Rev. B **58**, 497 (1998).
[19] M. Smidman, D. T. Adroja, A. D. Hillier, L. C. Chapon, J. W. Taylor, V. K. Anand, R. P. Singh, M. R. Lees, E. A. Goremychkin, M. M. Koza, V. V. Krishnamurthy, D. M. Paul, and G. Balakrishnan, Phys. Rev. B **88**, 134416 (2013).
[20] A. D. Hillier, D. T. Adroja, P. Manuel, V. K. Anand, J. W. Taylor, K. A. McEwen, B. D. Rainford, and M. M. Koza, Phys. Rev. B **85**, 134405 (2012).
[21] D. I. Khomskii, *Basic Aspects of the Quantum Theory of Solids: Order and Elementary Excitations* (Cambridge University Press, Cambridge, UK, 2010).
[22] S. Blundell, *Magnetism in Condensed Matter*, Oxford Master Series in Condensed Matter (Oxford University Press, Oxford, UK, 2001).
[23] F. L. Pratt, J. Phys.: Condens. Matter **19**, 456207 (2007).
[24] S. M. Disseler, C. Dhital, A. Amato, S. R. Giblin, C. de la Cruz, S. D. Wilson, and M. J. Graf, Phys. Rev. B **86**, 014428 (2012).
[25] D. T. Adroja, A. D. Hillier, J.-G. Park, W. Kockelmann, K. A. McEwen, B. D. Rainford, K.-H. Jang, C. Geibel, and T. Takabatake, Phys. Rev. B **78**, 014412 (2008).
[26] S. Lovesey, *Theory of Neutron Scattering from Condensed Matter* (Oxford University Press, Oxford, UK, 1984).
[27] V. K. Anand, D. T. Adroja, A. D. Hillier, J. Taylor, and G. André, Phys. Rev. B **84**, 064440 (2011).
[28] D. T. Adroja and V. K. Anand, Phys. Rev. B **86**, 104404 (2012).

[29] K. Stevens, Proc. Phys. Soc., London, Sect. A **65**, 209 (1952).
[30] K. Stevens, Rep. Progr. Phys. **30**, 189 (1967).
[31] J. Jensen and A. R. Mackintosh, *Rare Earth Magnetism* (Clarendon, Oxford, UK, 1991).
[32] Y. Koshikawa, H. Onodera, M. Kosaka, H. Yamauchi, M. Ohashi, and Y. Yamaguchi, J. Magn. Magn. Mater. **173**, 72 (1997).
[33] F. Strigari, T. Willers, Y. Muro, K. Yutani, T. Takabatake, Z. Hu, Y.-Y. Chin, S. Agrestini, H.-J. Lin, C. T. Chen, A. Tanaka, M. W. Haverkort, L. H. Tjeng, and A. Severing, Phys. Rev. B **86**, 081105 (2012).
[34] D. D. Khalyavin, A. D. Hillier, D. T. Adroja, A. M. Strydom, P. Manuel, L. C. Chapon, P. Peratheepan, K. Knight, P. Deen, C. Ritter, Y. Muro, and T. Takabatake, Phys. Rev. B **82**, 100405 (2010).